

# Influence of microstructure on fatigue of biocompatible $\beta$ -phase Ti-45Nb<sup>☆</sup>

M. Delshadmanesh<sup>a,\*</sup>, G. Khatibi<sup>a</sup>, M. Zare Ghomsheh<sup>b</sup>, M. Lederer<sup>a</sup>, M. Zehetbauer<sup>b</sup>,  
H. Danninger<sup>a</sup>

<sup>a</sup> Institute of Chemical Technologies and Analytics, Vienna University of Technology, Getreidemarkt 9/164, A-1060 Vienna, Austria

<sup>b</sup> Physics of Nanostructured Materials, Faculty of Physics, University of Vienna, Boltzmanngasse 5, 1090 Wien, Austria

## ARTICLE INFO

### Keywords:

$\beta$ -phase Ti-45Nb alloy  
Ultrafine grained  
Biomaterial  
High cycle fatigue  
High pressure torsion

## ABSTRACT

Biocompatible  $\beta$ -phase Ti-45Nb (wt%) alloy with a low elastic modulus of about 65 GPa has been proposed as suitable candidate for use in load bearing implants under fatigue conditions. In this work the influence of grain size on the mechanical properties and high cycle fatigue response of Ti-45Nb alloy has been studied. Severe plastic deformation was applied by using the high pressure torsion (HPT) technique in order to obtain an ultrafine grained (UFG) Ti-45Nb alloy with enhanced mechanical properties without increasing the elastic modulus. Due to limited size of the HPT processed samples, tensile and fatigue tests on the UFG and the initial conventional grained (CG) material were performed using small-scaled specimens and special testing set-up. Finite element simulations were conducted for calculation of the stress and strain conditions in the miniaturized samples subjected to dynamic loading. Grain refinement resulted in a mechanically stable structure with a considerable improvement of the tensile properties, however a significant improvement of the high cycle fatigue performance in comparison with the CG alloy was not observed. In order to explain this behavior, the changes in the nanohardness, subgrain size and dislocation density of the UFG material before and after SPD processing were evaluated and discussed. Microstructural investigations and fracture surface analyses were performed to gain information about the mechanisms of fatigue of the material at high cycle regime.

## 1. Introduction

Titanium alloys, stainless steels and Co-Cr alloys with biomechanical and biochemical compatibility are used for fabrication of a large variety of medical implants [1–3]. Especially  $\alpha + \beta$  type titanium alloys such as Ti-6Al-4V with excellent combination of mechanical properties and biocompatibility have been recognized as suitable candidates for bone implants. Their Young's moduli ( $\sim 110$  GPa) are, however, still greater comparing with that of the cortical bone (10–30 GPa) [4]. For structural biomaterials used in implants that replace hard tissue, a combination of enhanced tensile, fatigue and wear properties with low elastic moduli is desired. If the Young's modulus of a load bearing implant made of metallic biomaterials is higher than that of the cortical bone, bone atrophy may occur because of the stress shielding between the implant and bone [5]. Stress shielding causes loosening of the implants such as artificial joints or bone re-fracture after extraction of the implants [6]. Theoretical study of the effects of alloying elements on the strength and modulus of  $\beta$ -type bio-Ti alloys suggests that non-toxic and non-allergenic elements like Nb, Mo, Zr and Ta promote formation of  $\beta$ -type Ti alloys with enhanced strength and reduced Young's modulus

[7]. These alloys are especially suitable for use in load bearing implants under fatigue conditions such as artificial hip joints, bone plates and screws, spinal instruments, and dental implants [8–11]. Among the  $\beta$ -type titanium alloys with a bcc lattice, those based on Ti-Nb with a single  $\beta$ -phase, have significantly lower elastic moduli. Previous studies have shown a composition dependency of the Young's modulus of different stable and metastable phases for Ti-Nb binary alloys [12]. A minimum in Young's modulus of 62 GPa was observed at around the composition of Ti-45 mass %Nb in the single  $\beta$ -phase region [12–14]. Ti-45Nb alloy allows stabilizing a single  $\beta$ -type phase with low Young's modulus at room temperature. The Ti-Nb system is a well-established thermodynamic system, since it is of interest for a variety of applications. Earlier studies refer to an application of these alloys as superconducting material [15].

For the long term usage of metallic implants, biomechanical properties should be enhanced. Improvements in the static strength of biomaterials such as the tensile strength can be achieved by employing strengthening mechanisms including work hardening, grain refinement, precipitation and dispersion hardening. Severe plastic deformation (SPD) processes are defined as metal forming processes to fabricate

<sup>☆</sup> Dedicated to Prof. Hael Mughrabi on the occasion of his 80<sup>th</sup> birthday.

\* Corresponding author.

E-mail addresses: [mitra.delshadmanesh@tuwien.ac.at](mailto:mitra.delshadmanesh@tuwien.ac.at) (M. Delshadmanesh), [golta.khatibi@tuwien.ac.at](mailto:golta.khatibi@tuwien.ac.at) (G. Khatibi).

ultrafine-grained (UFG) materials, via introducing extremely high plastic strains into a bulk metal without any significant change in the overall dimensions. Within the available techniques equal-channel angular pressing (ECAP) and high pressure torsion (HPT) are efficient SPD techniques which usually require considerably smaller total strain to achieve the desired submicron grain sizes [16,17]. From a technological point of view, the structural application of HPT processed materials should be based on understanding and knowledge of their fatigue performance. Due to grain refinement and increased tensile properties of UFG metallic materials, an enhanced fatigue life in comparison with their equivalent conventional grained (CG) materials might be expected. Previous investigations have shown that the anticipated improvement in fatigue life is highly dependent on the used basic (initial) material [18–21].

In the present study, mechanical properties and fatigue performance of biocompatible  $\beta$ -Ti-45Nb alloy was investigated. High pressure torsion (HPT) was applied to enhance the tensile properties of the alloy without increasing the Young's modulus. Considering the few number of studies on fatigue of  $\beta$ -type titanium alloys for biomedical applications, the fatigue response of  $\beta$ -Ti-45Nb in the initial state and after HPT deformation was investigated. Since at present HPT processing can only be implemented for small samples (discs with less than 30 mm  $\phi$ ), all the experiments were conducted by using miniaturized specimens. Furthermore, two types of sample geometries were chosen, in order to consider the design aspects of the medical implants.

## 2. Materials and methods

### 2.1. Samples

The alloy investigated in the present work was a hot hydrostatic extruded (HHE)  $\beta$ -type Ti-45Nb (wt%) alloy provided as bars with a diameter of 42 mm and chemical composition as given in Table 1 received from ATI Wah Chang, Alabama, USA. The studies were performed on the samples prepared from the conventional grained original alloy and ultrafine grained HPT processed material which are denoted by CG and UFG, respectively.

The principle of HPT is illustrated schematically in Fig. 1. The disc which is located in a closed die is compressed by a very high pressure, and plastic torsional straining is achieved by rotation of one of the anvils. The equivalent strain according to the von Mises yield criterion is given by  $\epsilon = 2\pi Nr/h\sqrt{3}$ , where  $r$  is the radius of the disc,  $N$  the number of rotations and  $h$  the final thickness of the disc after HPT deformation [22]. In this work, slices with a thickness of about 0.8 mm and diameter of 8 mm were cut from the Ti-45Nb material normal to the axis of the bars. The Ti-45Nb discs were deformed under a hydrostatic pressure of 4 GPa and  $N = 1, 5$  and 10 at room temperature leading to an equivalent strain ( $\epsilon$ ) of 16, 82 and 170 at a radius of 2 mm from the center of the specimen. In all the cases the rotation speed was maintained to 0.2 rpm (revolutions per minute). Thickness of the samples after doing HPT processing of different number of rotations of  $N = 1, 5, 10$  was in the range of 0.45–0.49 mm.

Due to the limited size of the HPT processed discs (diameter of 8 mm), miniaturized tensile and fatigue samples were prepared by using special spark erosion cutting tools. Dumbbell shaped samples with a cross section of 0.75 mm  $\times$  0.45 mm and a gauge length of 2.5 mm were used for tensile tests (Fig. 2a). Fatigue experiments on the

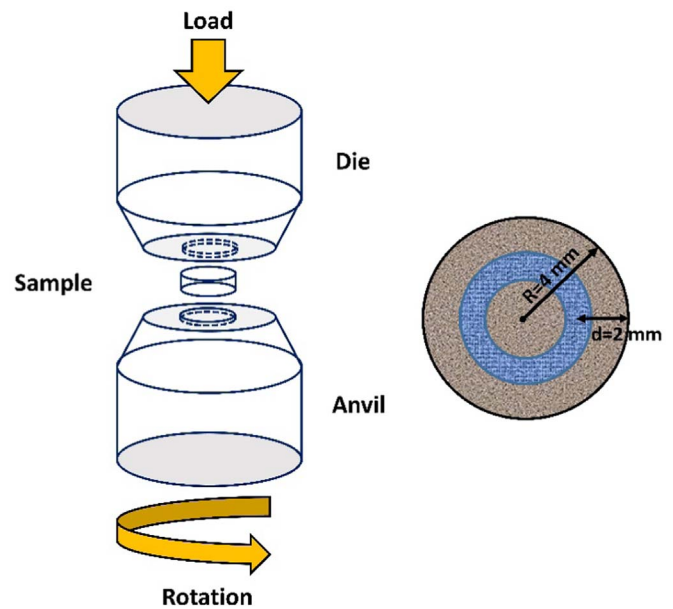


Fig. 1. The principle of HPT deformation processing (schematic), the samples were prepared from the blue area indicated on the HPT disc ( $\epsilon = 82$ ). (For interpretation of the references to color in this figure legend, the reader is referred to the web version of this article).

CG material were conducted by using hourglass and double-edge notched specimens and the UFG material was tested by using the hourglass sample geometry with the dimensions given in Fig. 2b and c. Both sample series had a gauge section of about 350  $\mu$ m and a thickness of 0.2 mm. The UFG samples were cut at the radius of about 2 mm from the center of the HPT discs to assure a similar microstructure at the gauge section as indicated with blue color in the disc illustrated in Fig. 1. All samples were mechanically thinned and fine polished with diamond paste to remove possible damages and to obtain smooth surfaces.

### 2.2. Microstructure and texture

A Bruker-AXS Discovery 8 X-ray diffractometer with a 2D detector using Cu  $K\alpha$  source with an accelerating voltage of 40 kV and a current of 30 mA was used for the analyses of composition of phases. Optical, scanning and transmission electron microscopy methods (OM, SEM, TEM) were used to reveal the microstructure and grain size distribution of the initial and HPT Ti-45Nb samples. The microstructure of the initial alloy was characterized with a scanning electron microscope type FEI Quanta 200 FEG by using Electron backscatter diffraction (EBSD) technique. TEM investigations were conducted by using a transmission electron microscope type FEI Technai F 20.

The dislocation density of the HPT Ti-45Nb samples before and after fatigue processing was measured by high-resolution diffraction peak-profile analysis [23,24]. The X-ray data were recorded using a highly monochromatic X-ray beam (with  $d\lambda/\lambda = 10^{-4}$ ) with a Curved Position Sensitive Detector INEL CPS-590 positioned at a distance of 480 mm from the specimen and Cu anode generator at 45 kV and 80 mA with a Ge single crystal monochromator. The line profiles were evaluated using the extended convolutional multiple whole profile (CMWP) procedure [25,26]. The distances between the specimen and detector were selected such that the instrumental effect was always < 10% of the physical broadening. The photon energy used was 8 keV, which corresponds to a wave length of Cu  $K\alpha_2$  radiation of 0.154 nm. The incident beam size was about 100  $\mu$ m  $\times$  500  $\mu$ m on the sample and the photon flux amounted to  $5 \times 10^{11}$  photons  $\text{mm}^{-2} \text{s}^{-1}$ . In case of fatigued and failed specimens, the X-ray beam was positioned on the middle of the plane surface of one of the broken parts and these results

Table 1  
Chemical composition of the Ti-45Nb alloy.

Element	wt%	at%
Ti	53.92	69.22
V	0.51	0.62
Nb	45.57	30.16

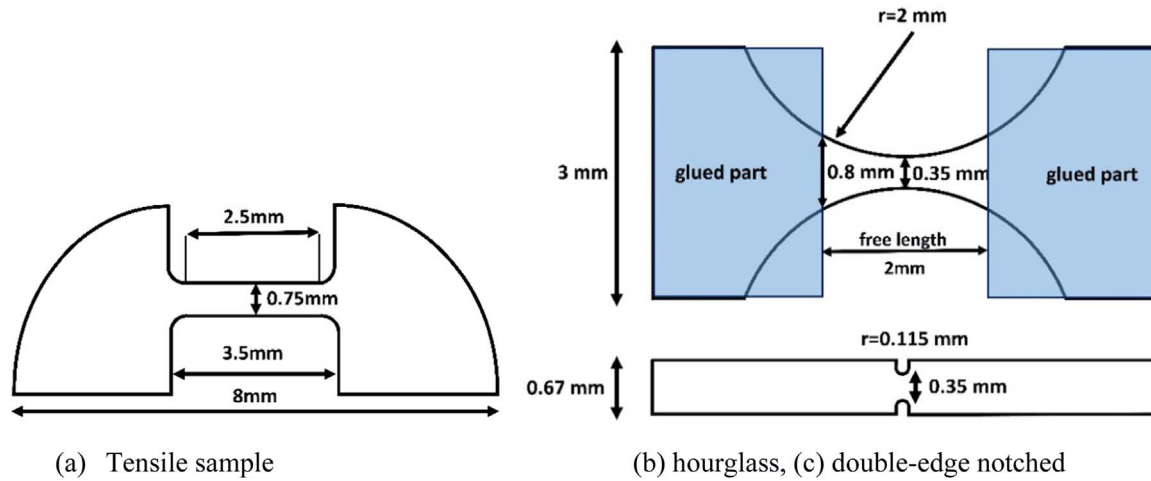


Fig. 2. a, b, c: Schematic of tensile and fatigue samples. (a) Tensile sample (b) hourglass, (c) double-edge notched.

**Table 2**  
Mechanical properties of the CG and UFG (HPT P = 4, N = 5) Ti-45Nb specimens.

Sample	Dislocation density [ $1/\text{m}^2$ ]	Young's modulus [GPa]	UTS [MPa]	Yield strength [MPa]	Average grain size [ $\mu\text{m}$ ]	Nanohardness [GPa]	Fracture strain %
CG	$1.35\text{E}+15$	$65.4 \pm 2.1$	$446 \pm 12$	$430 \pm 21$	20 $\mu\text{m}$	$1.42 \pm 0.02$	21.8
UFG	$3.30\text{E}+15$	$67.7 \pm 2.1$	$940 \pm 14$	$864 \pm 25$	< 0.100	$2.42 \pm 0.04$	9.4

will be presented and discussed in the last section. The measured dislocation density for the CG and UFG samples before fatigue testing are presented in Table 2.

Fig. 3 presents the phase compositions of the Ti-45Nb samples at the initial state and after HPT deformation at 4 GPa hydrostatic pressure and by 5 rotations. The XRD results confirm that both initial CG and UFG Ti-45Nb samples consist of a single  $\beta$ -phase and no phase transformation occurred during HPT processing (Fig. 3). Fig. 4a shows the grain size distribution and the texture of the initial Ti-45Nb alloy normal to the axis of the bar (OM). TEM dark and bright field images of the microstructure of Ti-45Nb after HPT deformation and the corresponding selected area electron diffraction (SAD) pattern are shown in the Fig. 4b, c and d. HPT deformation of the initial sample with an average grain size of about 20  $\mu\text{m}$  resulted in an ultrafine grained microstructure with grain size of less than 100 nm. The continual diffraction rings of the  $\beta$ -phase shown in Fig. 4c confirm the results of XRD

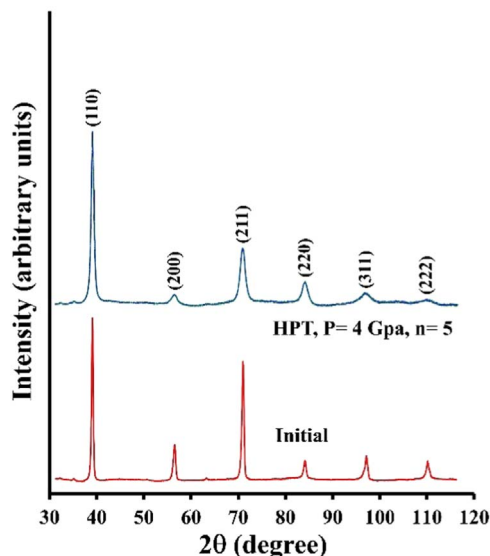


Fig. 3. XRD spectrum for the initial state and HPT (n = 5, p = 4 GPa) samples.

measurements.

### 2.3. Mechanical properties

Nanoindentation techniques and tensile tests were performed for characterization of the mechanical properties of the CG and UFG samples. Nanoindentation measurements were conducted to study the effect of HPT processing parameters on the values of nanohardness and Young's modulus of the Ti-45Nb alloy. The measurements were carried out at room temperature by an ASMEC-Universal Nanomechanical Tester UNAT and using a Vickers indenter. The device was calibrated in terms of indenter stiffness and contact area using fused silica and sapphire standards. The measurements were carried out on the HPT discs on an area with the radius ranging from 2/5R to 3/5R as shown in Fig. 1b (marked with blue color). About 50 single measurements were performed on each material from which an average value was obtained. Young's modulus was determined according to the methods given by Oliver and Pharr [27]. Typical nanoindentation load displacement curves for Ti-45Nb alloy obtained for the CG and UFG materials after different stages of HPT processing are presented in Fig. 5. The corresponding values of elastic modulus and nanohardness are demonstrated in Fig. 6a and b showing the evolution of these both values with increasing the degree of shear deformation. The results show that the value of Young's modulus after HPT deformation is only slightly higher than the value measured for the CG samples, while a considerable increase of nanohardness from 1.42 for CG sample to 2.42 for UFG material after 5 rotations is observed.

Tensile tests were performed with a strain rate of  $10^{-3}/\text{s}$  using a miniaturized tensile machine with a load cell capacity of 2 kN equipped with non-contacting laser speckle sensors based on the correlation technique [28]. Typical stress-strain curves of the initial and UFG Ti-45Nb samples are presented in Fig. 7. It can be seen that, HPT deformation leads to a strong increase in the ultimate tensile strength about 100% from 446 MPa for the CG to 940 MPa for the UFG sample. The tensile tests also show a reduction of the fracture strain from above 20% to about 10% after HPT deformation.

The results show that HPT processing induced a significant increase in the strength of the Ti-45Nb alloy while maintaining the Young's

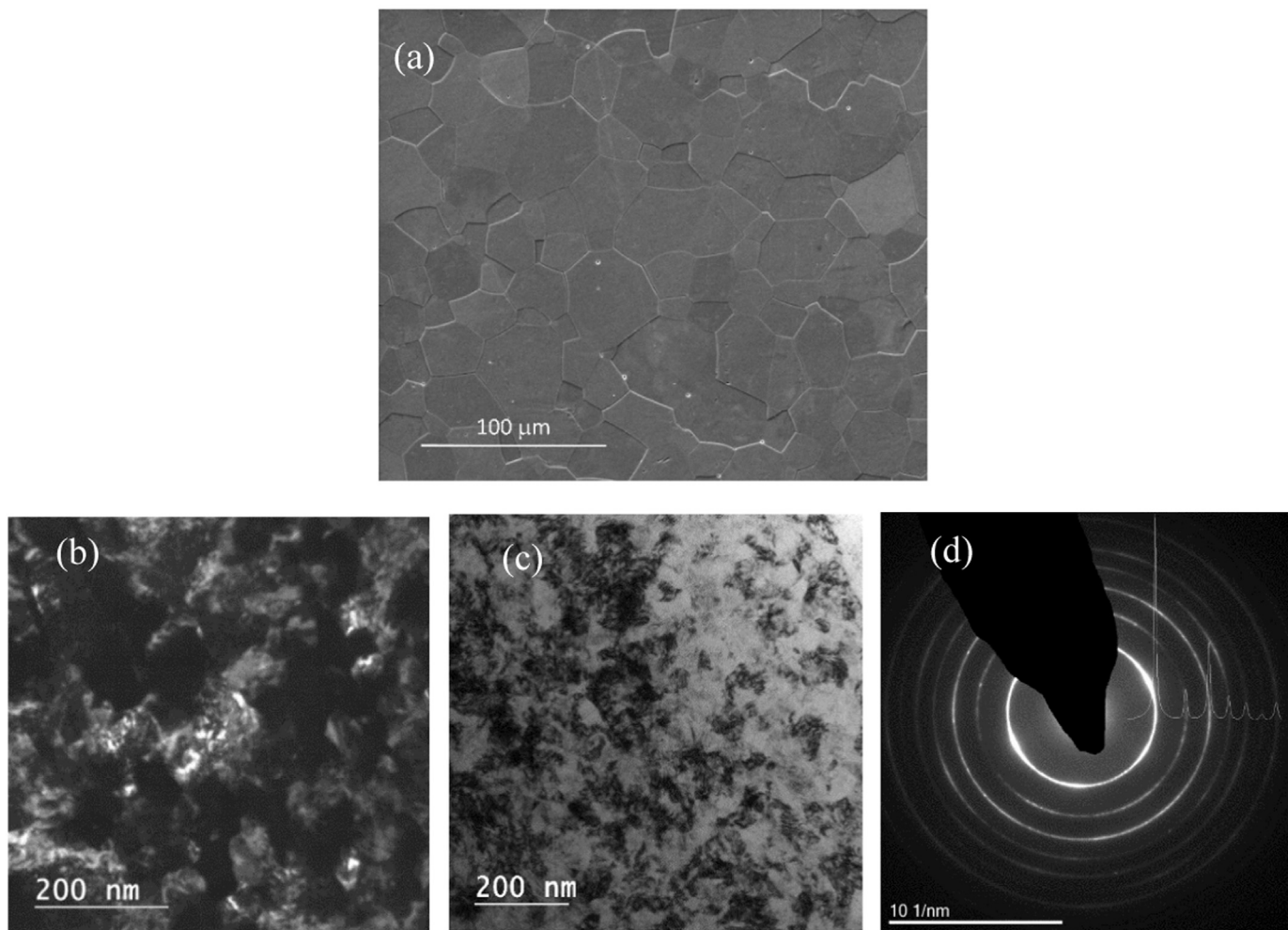


Fig. 4. Microstructure of Ti-45Nb material, a) conventional grained initial alloy, b, c and d) Ultrafine grained material (UFG) processed by HPT with  $P = 4$  GPa,  $n = 5$ ; (b, c) dark and bright field TEM images and the (d) corresponding selected area electron diffraction (SAD) pattern of the beta phase.

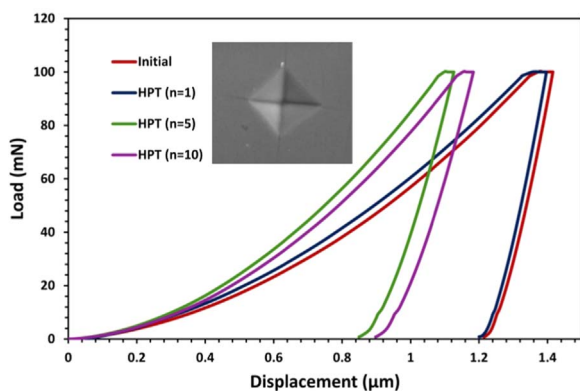


Fig. 5. The plot of load versus displacement curves with  $F_{max} = 100$  mN and Vickers indenter. Inset figure shows typical indent made by Vickers indenter.

modulus at the low level of the initial material. With regard to the obtained values of Young's modulus and nanohardness for the HPT processed alloy at three different number of rotations ( $N = 1, 5, 10$ ) and 4 GPa hydrostatic pressure and since the increasing of the tensile strength and nanohardness are rather saturated after HPT of 5 rotations (Fig. 6a and b) for this study the HPT Ti-45Nb material processed under 5 rotations was selected for the fatigue investigations.

A summary of the microstructural and mechanical properties of the initial CG and UFG Ti-45Nb samples is presented in Table 2.

#### 2.4. Fatigue experiments

Since skeletal implants are frequently exposed to long-term cyclic loading [29], our investigations concentrated on the high cycle fatigue regime up to  $10^9$  cycles. A special testing system composed of an ultrasonic resonance fatigue testing system working at 20 kHz in combination with a special experimental set up already developed for testing of miniaturized specimens was used to perform fatigue tests. For fully reversed loading condition ( $R = -1$ ), the mechanical system is composed of a piezoelectric transducer, an amplification horn, and a specimen holder. The distribution of displacement and strain varies sinusoidally along the system with the maximum strain being in the midsection of the specimen holder (Fig. 8). A bar shaped specimen holder of high strength Ti-alloy with a cross section of  $20 \text{ mm} \times 8 \text{ mm}$  and a resonance length of 128 mm containing a through hole with a diameter of 2 mm in the midsection was used for fatigue testing. The miniaturized specimens were aligned and glued carefully over the notch of the holder parallel to the loading direction by using a cyanide-acrylate adhesive. The gauge section of the miniaturized specimen across the hole is freestanding in this location. Strain measurements were performed by using miniature strain gauges. The velocity of vibration at the end of the sample holder was measured by using a laser Doppler Vibrometry (LDV) during the loading. During testing, a video camera attached to a light microscope was used to monitor the plane surface of the specimens. This allowed recording the entire fatigue process and determination of the number of loading cycles ( $N_f$ ) to failure.

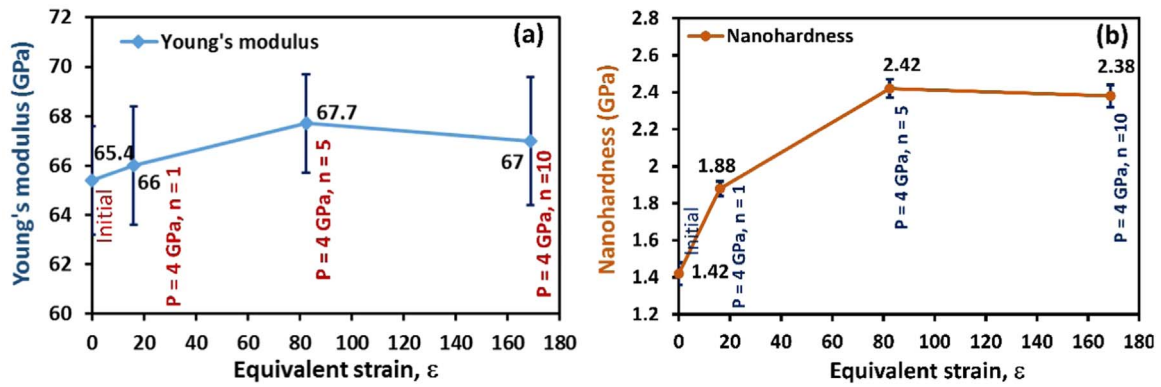


Fig. 6. Nanoindentation results of initial and HPT Ti-45Nb; (a) Young's modulus and (b) Nanohardness values vs. equivalent strain.

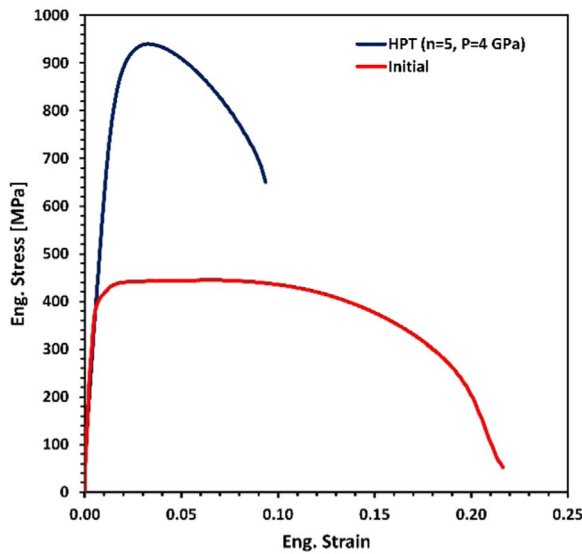


Fig. 7. Stress-strain curves of initial and HPT Ti-45Nb specimens.

Compressed air cooling prevents heating of the sample and a light microscope is used to observe the sample surface. The magnification of the microscope and the video system could be set up to 1000× with a resolution of about ± 5 μm. Tests were performed at room temperature with additional cooling of the specimen by pressurized dry air. Control temperature measurements were performed using an infrared thermometer with a spot size of about 0.6 mm on the surface of specimens to ensure the room temperature testing conditions.

2.4.1. Strain and stress calibration

Strain and displacement measurements were used for the calibration of the fatigue experimental set-up and determination of the relationship between the strain values at the plane surface of the test specimens to

that of the specimen holder. Strain gauges were attached to the gauge section of the specimen and to the site of maximum strain on the side face of the specimen holder. Due to the small geometries of the notched and hourglass shaped samples with thickness of 200 μm and gauge section of about 350 μm direct strain measurements by application of commercially available strain gauges was not possible. Therefore, strain measurements were performed by using calibration hourglass samples with the same thickness and a width of about 600 μm in the gauge section. The displacement/strain amplitude was increased stepwise and the ratio of the strain value at midsections of the miniaturized sample to the holder was determined. The experimental strain ratio ( $R_E = \epsilon_{sample} / \epsilon_{holder}$ ) was determined by linear regression as shown in Fig. 9. The obtained value of 2 which is lower than the theoretical  $K_t = 2.73$  (for a rectangular bar of 20 mm with a through hole of 2 mm) corresponds to the actual increase of stress on the free standing samples glued to the holder across the hole.

The corresponding stress amplitude of the specimens was calculated based on the experimental calibrations and Finite Element Analysis (FEA). The experimental stress value was determined by using the strain measured at the mid-section of the holder at each stress amplitude, the obtained strain calibration factor and the theoretical stress concentration factors for each sample geometry. Under the assumption of preliminarily elastic deformation of the specimen at HCF region Hooke's equation was used:

$$\frac{\Delta\sigma}{2} = R_E \cdot K_t \cdot E \cdot \left(\frac{\Delta\epsilon}{2}\right)_{holder} \tag{1}$$

where E is the elastic modulus of the Ti-45Nb alloy,  $\left(\frac{\Delta\epsilon}{2}\right)_{holder}$  is the strain at the side face of the specimen holder,  $K_t$  is theoretical net stress concentration factor according to Peterson [30] and  $R_E$  is the calibration factor measured by the strain gauges.

3. Finite element analysis

Finite element analysis (FEA) was performed by using ANSYS

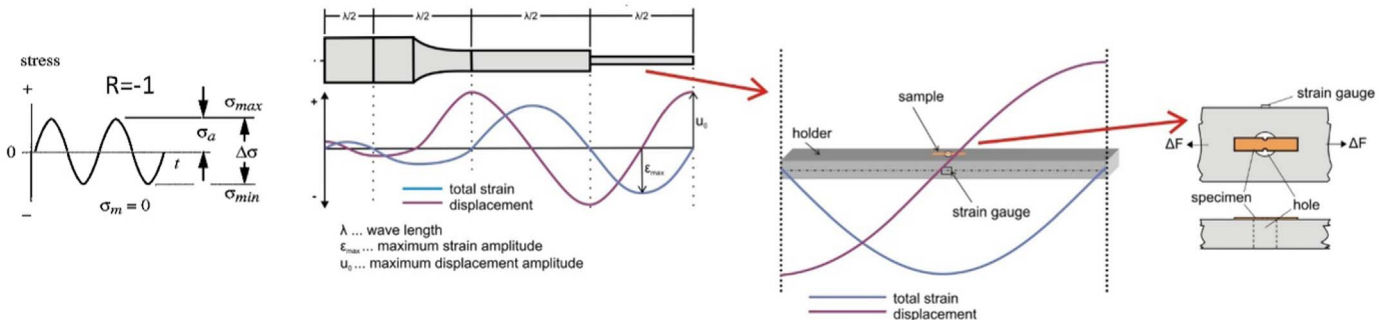


Fig. 8. Schematic of principal of ultrasonic fatigue technique and experimental set up for miniaturized specimens under fully reversed loading condition ( $R = -1$ ).

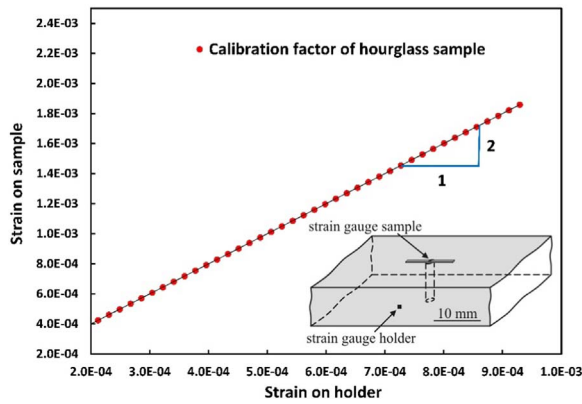


Fig. 9. Calibration curves for determination of strain in the miniaturized samples.

**Table 3**  
Summary of strain calibration measurements.

Sample shape and width	$K_{tn}$	$R_E \times K_{tn}$	$K_{t-Dyn}$	$R_{FA}$
Hour-glass, 0.6 mm	1.18	2.36	3.44	2.80
Hour-glass, 0.35 mm	1.05	2.10	3.91	3.42
Double-edge notched, 0.35 mm	1.83	3.66	7.53	3.32

$R_E$ : experimentally determined strain ratio ( $\epsilon_{sample}/\epsilon_{holder} = 2$ ).

$R_{FA}$ : volume averaged strain ratio calculated by FEM ( $\epsilon_{yy\ sample}/\epsilon_{yy\ holder}$ ).

$K_t$ : analytical net stress concentration factor.

$K_{t-Dyn}$ : stress concentration factor calculated by FEM (max.v. Mises strain).

software in order to calculate the distribution of strain and stress in the miniaturized samples. The mesh size and geometry of the models was selected in a manner to define the contours of the miniaturized samples properly. Thereby, the mesh was refined in the region around a notch wherever this was necessary. FE models were constructed for three geometries including the calibration sample, hourglass shaped and double edge notched samples with details listed in Table 3 and Fig. 2b and c. Harmonic analyses were conducted by adjusting the sinusoidal loads in order to fit the measured displacement amplitude at the end of the sample holder which corresponds to the strain amplitude at the midsections of the holder. Using these data, the ratio of the calculated strains of the sample at different locations to the strain measured in the midsection of the side face of the holder was determined. The calculated strain in the miniaturized samples is also influenced by the geometry of the experimental set-up. In particular, stress concentrations are introduced by the hole in the midsection of the holder across which the samples are stretched due to attachment to the ambient periphery of the hole. Since the direction of loading is along the y-axis of sample and holder, particular interest was devoted to the strain component  $\epsilon_{yy}$  which was also measured by strain gauges. Furthermore, the simulations revealed that the value of the strain component  $\epsilon_{yy}$  was nearly identical with the value of von Mises strain which may be used as failure criterion. The calculated values include the ratios of i) the strain at the location of highest stress concentration which is found at the side faces of the samples (denoted as  $K_{t-dyn}$ ) ii) the volume averaged strain in the gauge section of the samples (denoted as  $R_{FA}$ ) to the calculated strain in the midsection of the side face of the holder (Fig. 8).

The strain distribution plots of the hourglass and double-edge notched miniaturized fatigue samples attached across the hole in the midsection of the holder are presented in Fig. 10a, c, e and b, d and f, respectively. The simulations show that the chosen experimental set-up results in a gradient of strain across the thickness of the samples ( $t = 200\ \mu\text{m}$ ), with the highest values being in the midsection of their lower surface as shown for the hourglass (Fig. 10c) and notched samples (Fig. 10d). The strain distribution in the plane normal to the loading direction shows the proportional contribution of the stress values in the gauge section of the samples (Fig. 10e, f) from which the volume

averaged strain was determined.

A summary of the experimental and theoretical strain ratios and stress concentration factors are given in Table 3. The results show that  $K_{t-Dyn}$  for the notched samples at the location of the highest stress concentration is  $\sim 7.5$  which is larger than the value of  $R_E \times K_t$  (see also Eq. (1)) by a factor of two. On the other hand, the values of  $R_E \times K_t$  show a better compliance with  $R_{FA}$  (calculated volume averaged strain ratio) for all sample geometries. It is known that analytical or numerical methods based on the theory of elasticity may result to an over-estimation of the stress concentration especially in the case of sharp notches due to neglecting the strain gradient effects. Therefore, in the present study the S-N curves were plotted by using the  $R_{FAve}$  factor for calculation of the volume averaged stress and the following formula:

$$\frac{\Delta\sigma}{2} = R_{FA} \cdot E \cdot \left( \frac{\Delta\epsilon}{2} \right)_{holder} \quad (2)$$

## 4. Experimental results

### 4.1. Fatigue life curves

S-N curves of miniaturized notched and hourglass shaped CG Ti-45Nb samples are shown in Fig. 11a and b. The plot displayed in Fig. 11a shows the raw experimental fatigue data without taking the stress concentration factors of the samples ( $K_t$ ) into account compared with those calculated on the basis of volume averaged stress (Eq. (2)). The stress amplitude given in the fatigue life curves presented in Fig. 11b is based on the maximum stress concentration in the gauge section of the notched and hourglass-shaped samples. S-N curves of CG samples of both geometries show a rather flat trend in the region of HCF ( $N > 1e5-1e9$ ). As expected, the fatigue life curves based on volume averaged stress (VAS) lie above the raw experimental curves and the notched specimens demonstrate a fatigue strength of about 45% lower than their hourglass shaped counterparts (Fig. 11a) for stress values determined by both methods. On the other hand, using the  $K_{t-Dyn}$  for estimation of the stress amplitude of the samples results in a higher lifetime for the notched samples than that of hourglass shaped ones with a considerable scattering of the fatigue data (Fig. 11b). Both trends are consistent with Weibull statistics considering the very small sample volume subjected to elevated stress in notched samples. In fact, the volume exposed to stress concentrations in miniaturized samples is so small that a variance of fatigue strength can be observed for the Ti-45Nb alloy.

In order to estimate the influence of stress concentration on the fatigue performance of the Ti-45Nb alloy it was attempted to determine the fatigue notch sensitivity factor of the CG material. The fatigue notch factor  $K_f$  is defined as

$$K_f = \sigma_{smooth} / \sigma_{notch} \quad (3)$$

with  $\sigma_{smooth}$  being the fatigue limit of unnotched bodies (hour glass shaped samples) and  $\sigma_{notch}$  being the fatigue limit of notched bodies. The fatigue notch sensitivity factor  $q$ , is obtained [31,32] according to the equation

$$q = \frac{K_f - 1}{K_t - 1} \quad (4)$$

where  $0 \leq q \leq 1$ .

The full notch sensitivity is given by  $q = 1$  ( $K_f = K_t$ ) and complete notch insensitivity is given by  $q = 0$  ( $K_f = 1$ ).

The fatigue notch factor was determined based on the measured and calculated stress amplitudes at  $1e9$  loading cycles with the values of  $K_f = 1.74$  (experimental stress amplitude ratio of 110/63) and  $K_t = 1.74$  (calculated stress amplitude (VAS) ratio of 186/107) presented in Fig. 10a. Considering the value of  $K_t = 1.83$  for the double edge notched samples after Peterson formula and the obtained experimental  $K_f$  value of  $\sim 1.7$  of this study the notch sensitivity factor is determined to

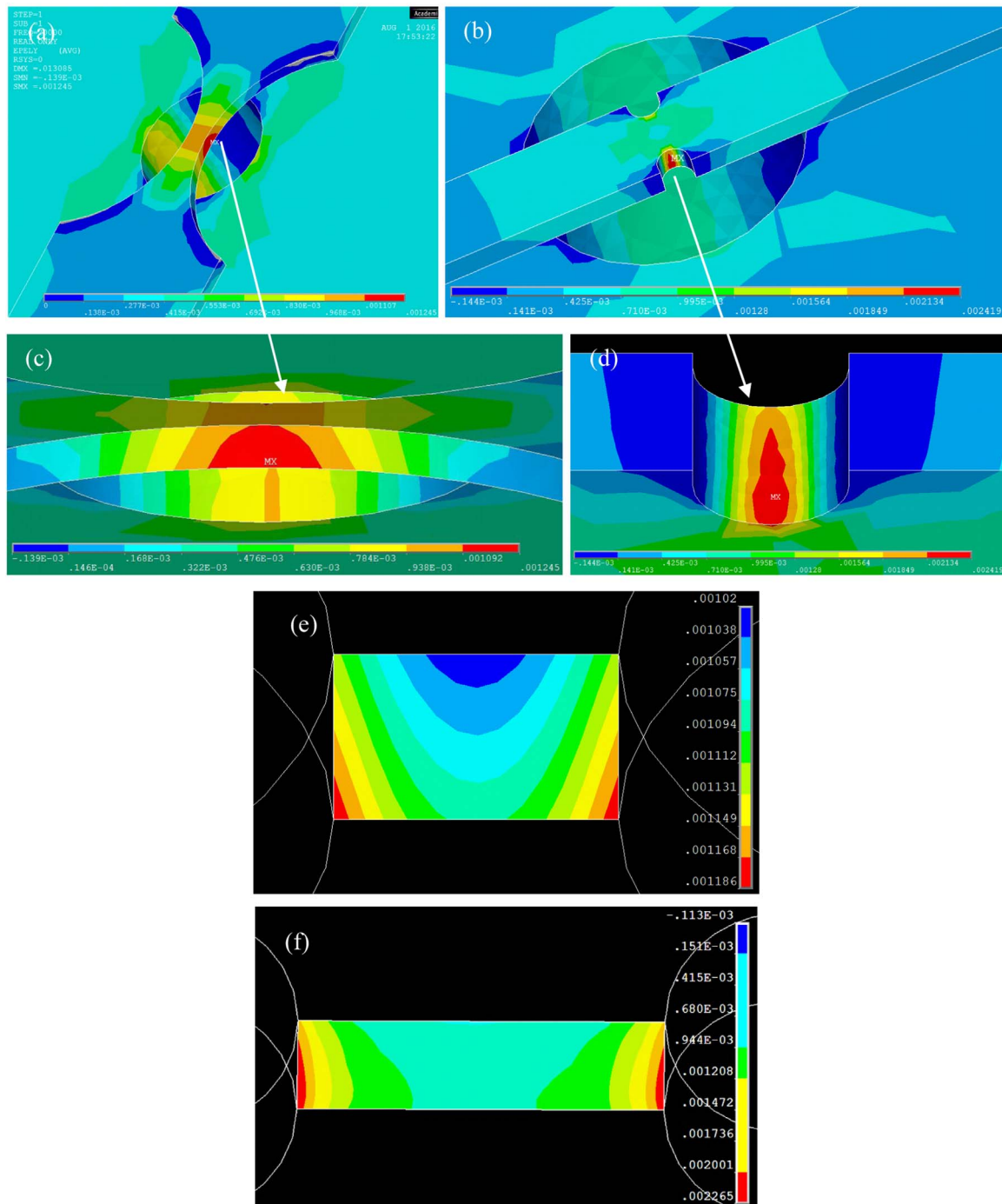


Fig. 10. Plots of strain distribution for (a, c) hourglass sample related to 845  $\mu$ strain on holder. Max. Strain: 0.33%. ( $K_t = 3.90$ ) (b, d) notched sample related to 321  $\mu$ strain on holder. Max. Strain: 0.33%; (e and f) strain distribution in the gauge section of (e) hourglass and (f) notched samples in the plane normal to the loading direction.

be  $q = 0.89$ . Consequently, the Ti-45Nb alloy with the given geometry and grain size of about 20  $\mu$ m can be considered as notch sensitive [33].

Recently the authors investigated the effect of notch geometry on the high cycle fatigue response of  $\beta$ -Ti-45Nb bulk alloy by using an ultrasonic fatigue testing system [34]. The fatigue resistance of hourglass shaped samples was determined to be 260 MPa at  $1e9$  cycles and the cycles to failure was highly dependent on the location of the defects. Presence of notches resulted in a strong drop of the lifetime curve and the fatigue notch sensitivity factor ( $q$ ) was found to be 0.95–0.76 depending on the notch geometry. The lower fatigue resistance of the smooth miniaturized samples of the present study with a rectangular cross section (186 MPa) in comparison with the bulk Ti-45Nb samples

with circular cross section [34] can be mainly explained by the influence of sample geometry. According to the cross-sectional stress distribution plots of Fig. 10e and f the stress at the edges of the rectangular shaped samples is considerably raised. Thus, for the notch sensitive material, the presence of these stress concentrators can lead to an earlier failure as also confirmed by the fracture surface analysis of the fatigued miniaturized samples.

The influence of grain refinement on the fatigue life of Ti-45Nb is presented in Fig. 12a with the stress amplitude being calculated based on the averaged v. Mises stress for the CG and UFG Ti-45Nb hourglass shaped samples. The endurance limit of UFG and CG material at  $1e9$  cycles are 200 MPa and 186 MPa respectively resulting a slight

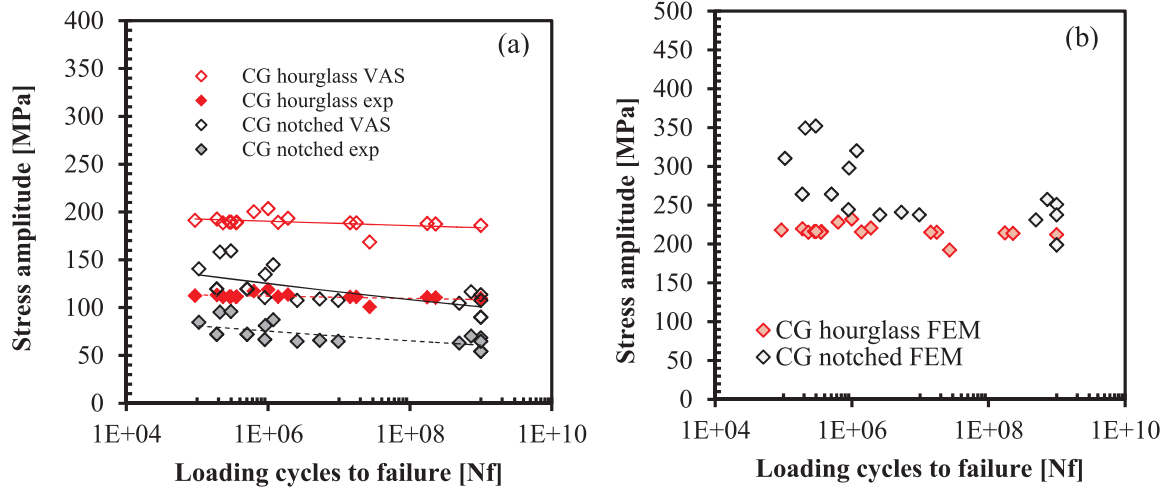


Fig. 11. Fatigue life curves of miniaturized notched and hourglass shaped CG Ti-45Nb samples a) experimental data without  $K_t$ , and volume average stress curves b) plotted based on the maximum stress (FEM).

improvement of fatigue resistance due to HPT processing. Typical fatigue crack paths of the samples are displayed in the plane views of failed CG (Fig. 12b) and UFG sample (Fig. 12c). The zigzag type and the straight crack path of the CG and the UFG samples respectively are in conformity with the commonly observed grain size dependent fatigue crack path morphologies in metallic materials (Fig. 12b, c).

The effect of severe plastic deformation on the improvement of fatigue resistance of metals has been subject of a large number of investigations [35–37]. It has been reported that the expected fatigue response is dependent on several factors including the purity and composition of the used material, processing conditions, fatigue testing conditions and also the anticipated fatigue regime [37–40].

In most cases, it is reported that grain refinement by SPD processing of alloys and low purity metals results in a significant enhancement of fatigue resistance under stress controlled testing conditions in the high cycle regime [41–44]. In our study, as already presented, grain refinement by HPT processing resulted in a considerable increase in the yield strength and tensile stress of the Ti-45Nb alloy (Table 1, Fig. 7). The fatigue limit at  $1e9$  cycles is in the range of 185–200 MPa for the CG and UFG samples which correspond to  $\frac{\sigma_s}{\sigma_f}$  (ratio of UTS to fatigue limit) of about 2.5 and 4.5 for the former and latter materials. Thus, considering that the maximum stress amplitude of the obtained S-N curve in the very high cycle regime (about 210 MPa) is far below the elastic limit of the UFG material ( $\sigma_y = 860$  MPa), the high cycle fatigue response of the UFG Ti-45Nb of this study is rather unexpected.

Generally, the moderate fatigue performance nanostructured or ultrafine grained materials processed by SPD has been related to the occurrence of cyclic softening due to the thermal and mechanical instability of the material. A further issue is the decreased ductility and the high crack growth rate in the materials with extremely fine microstructure [45–48]. For a better understanding and interpretation of the fatigue response of CG and UFG Ti-45Nb alloy of the present study, fatigue fracture surfaces of the CG and UFG samples are analyzed and the evolution of microstructure, hardness and dislocation density of the UFG samples with increasing the loading cycles are investigated in the following.

#### 4.2. Fracture surface analysis

Due to the flat trend of the obtained fatigue curves, the impact of the number of loading cycles to failure on the fracture behavior of the samples was studied. The fracture surfaces of CG samples which failed at almost the same stress amplitude and different loading cycles in the range of  $\sim 1e5$ – $1e8$  are presented in Fig. 13a, c, e. The corresponding details are shown in Fig. 13b, d and f. It can be observed that independent from the loading cycles all samples failed in a crystallographic appearance with crack initiation site being at the surface or close to the surface. Surface or internal defects were scarcely identified as sources of fatigue cracks. Fatigue crack in the specimens which failed earlier initiated mostly from their corners with cracks originating from

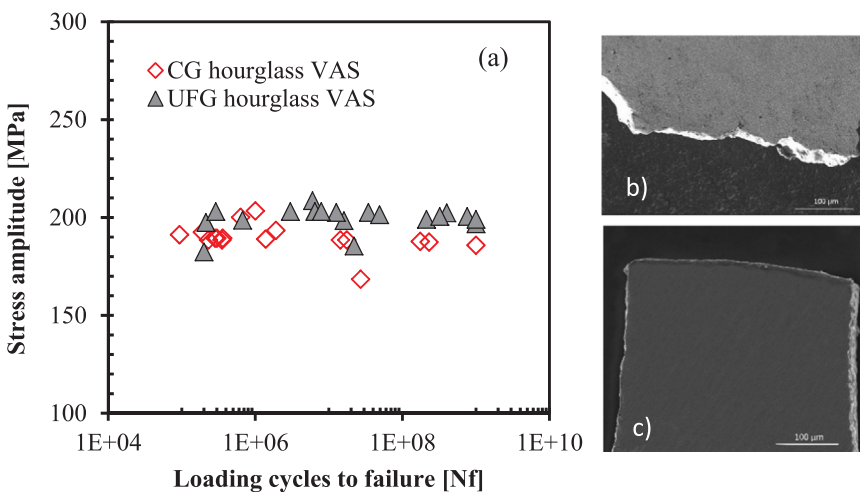
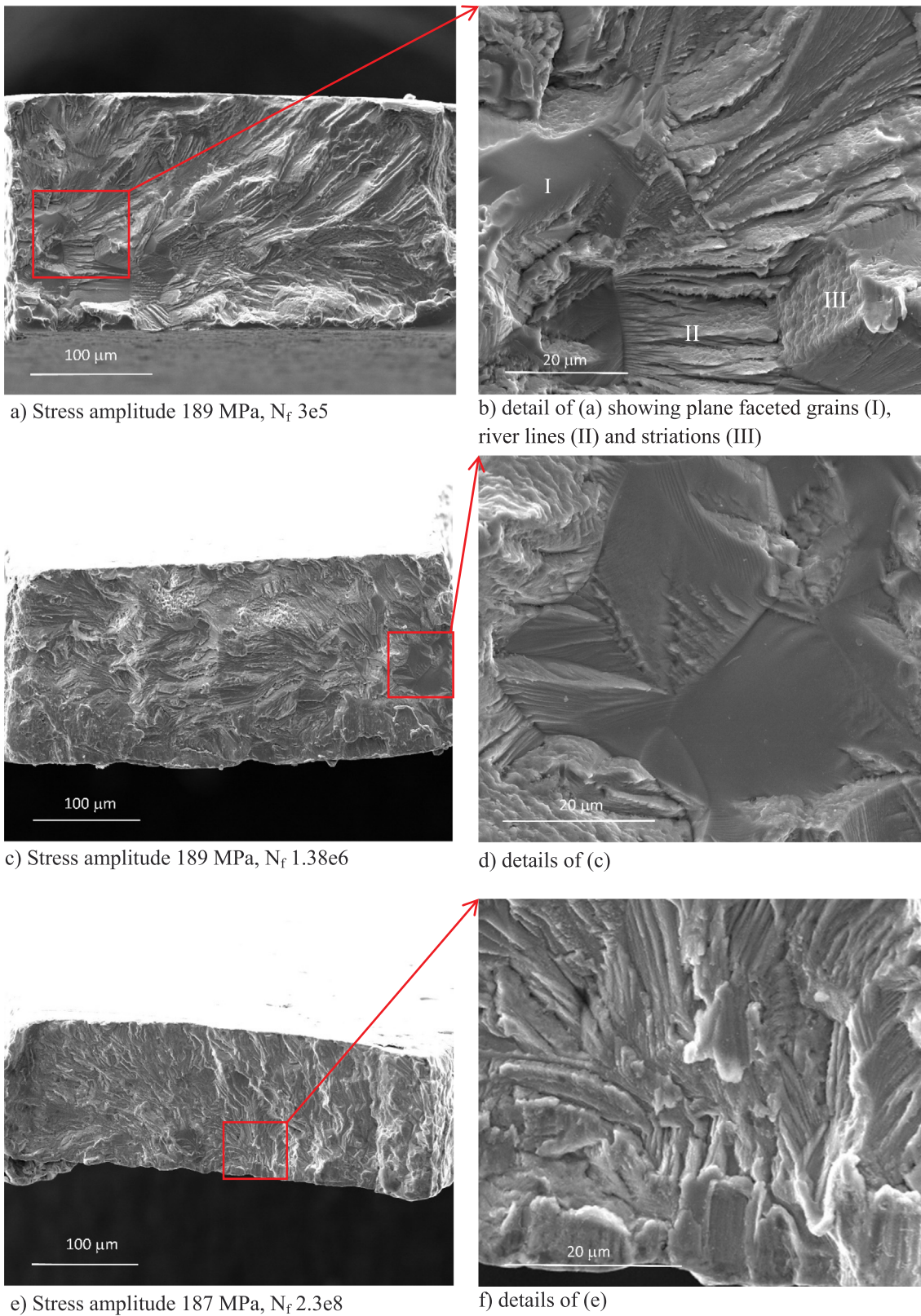


Fig. 12. a) S-N curves of miniaturized hourglass initial (CG) and HPT samples (UFG) which notch factor ( $K_t$ ) was calculated by FEM simulation ( $K_t = 3.90$ ). Plane view of failed (b) CG and (c) UFG Ti-45Nb fatigue samples.



a) Stress amplitude 189 MPa,  $N_f$  3e5

b) detail of (a) showing plane faceted grains (I), river lines (II) and striations (III)

c) Stress amplitude 189 MPa,  $N_f$  1.38e6

d) details of (c)

e) Stress amplitude 187 MPa,  $N_f$  2.3e8

f) details of (e)

Fig. 13. Fatigue fracture surfaces of coarse grained Ti-45Nb samples failed at about 234 MPa and different loading cycles, (a, c, e) overview and (b, d, f) detail SEM images.

cleavage of one or few grains at these sites and expanding radially across the surface (Fig. 13b, d). These plane faceted features were rarely observed on the samples which failed at higher loading cycles (Fig. 13e, f). The overall fracture morphology was a dominant quasi-cleavage type, which maintained its rough appearance throughout the sample.

Apparently, a transition of crack propagation mode I to mode II did not occur, however several grains contained fatigue striations as marked in Fig. 13b, d, f. The fracture appearance could be related to the small size of the samples, suppressing the fatigue crack growth phase resulting in a short time to failure after initiation of the fatigue crack.

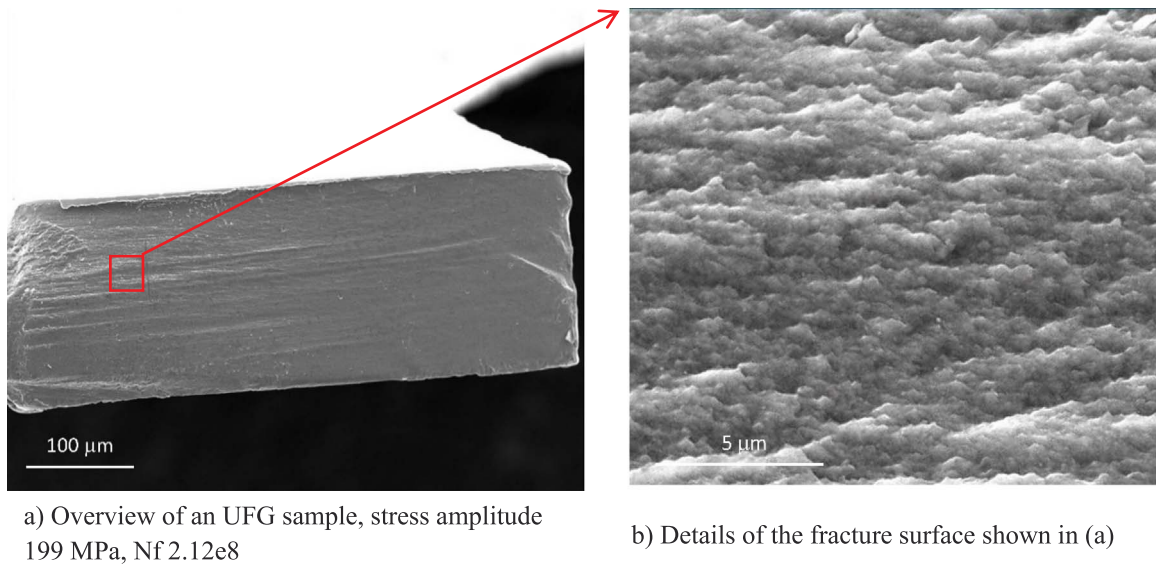


Fig. 14. Overview (a) and detail (b) of fatigue fracture surface of ultra-fine grained Ti-45Nb.

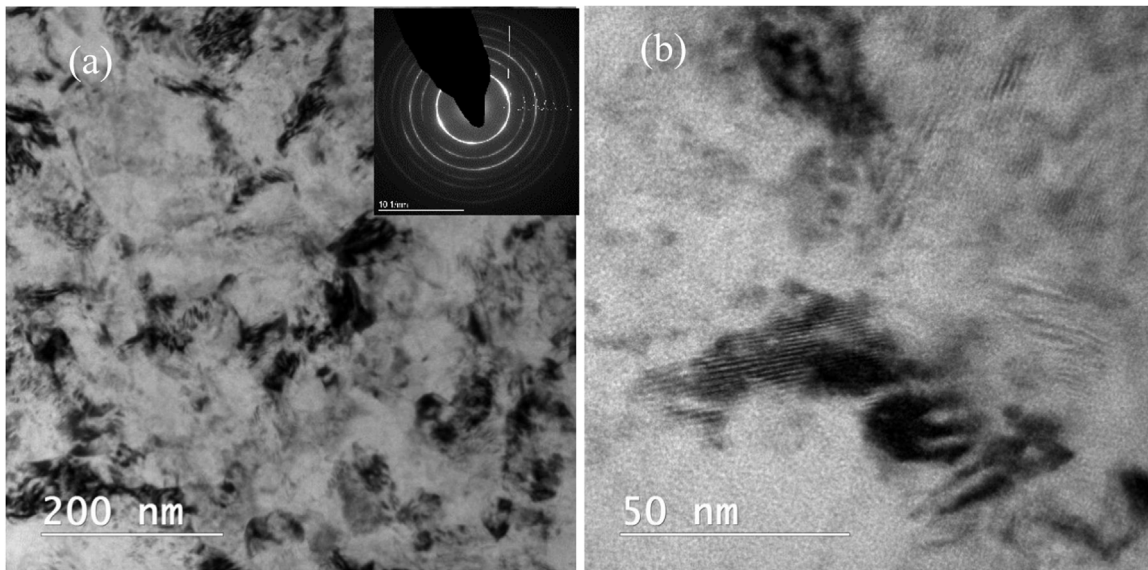


Fig. 15. Low (a) and high (b) magnification bright field TEM images of the microstructure of a run out UFG Ti-45Nb material (200 MPa, N = 1e9 loading cycles).

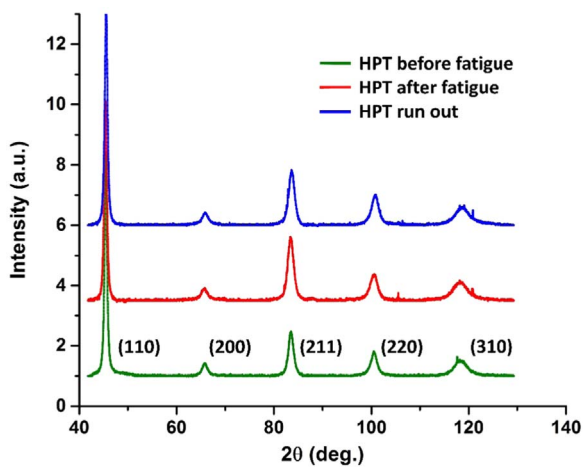


Fig. 16. Measured intensity profiles of HPT Ti-45Nb samples in three different states.

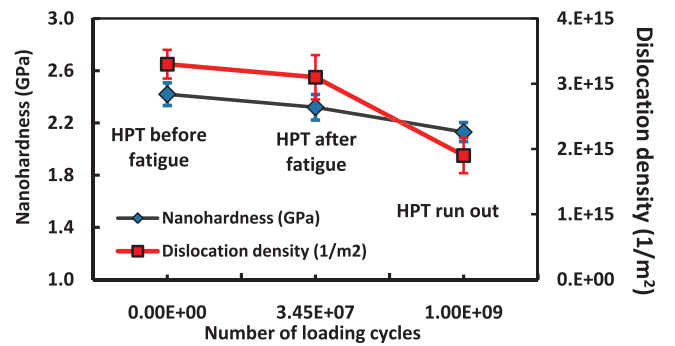


Fig. 17. Nanohardness and dislocation density of UFG material as a function of loading cycles.

Fig. 14a shows the overview of the fracture surface of long life UFG Ti-45Nb fatigue sample with the detail being displayed in higher magnification in Fig. 14b. Fatigue crack originates from the corners and propagates through the gauge section of the sample resulting in a flat

fracture surface morphology typical for UFG materials. Several fine lines expand across the cross section parallel to the surface of the sample in the shear plane of the HPT disc resulting in a step like appearance of fracture surface. The extremely fine parallel fatigue lines which run throughout the long life sample are shown at higher magnification in Fig. 14b. This image corresponds perfectly to the straight crack path observed on the plane surface of the UFG sample and indicates a rapid crack growth rate which might have resulted in a moderate fatigue resistance of UFG material. The low fatigue performance of the UFG samples can also be related to the fatigue notch sensitivity ( $q$ ) of the material and the chosen sample geometry. The rectangular cross section of the samples with edges acting as stress raisers which may promote early crack initiation in both CG and UFG Ti-45Nb samples (as also shown in the FEM plots). Considering the high value of  $q = 0.89$  obtained for the CG alloy of this study, and the commonly accepted trend of increased notched sensitivity with decreasing the grain size, a higher impact of the sample geometry on the fatigue response of the UFG Ti-45Nb may be expected [49,50].

#### 4.3. Analysis of the fatigue response of UFG Ti-45Nb

The microstructural stability of the HPT Ti-45Nb material during the dynamic loading was examined by means of TEM and X-ray diffraction analysis. TEM images of a run out UFG Ti-45Nb sample (Stress amplitude = 200 MPa and  $N = 1e9$ ) are presented in Fig. 15a and b. Careful microstructural examinations did not show evidence of noticeable changes in the grain size of material after long-term fatigue loading. Fig. 16 confirms that the measured intensity profiles of the UFG Ti-45Nb samples prior to and subsequent to fatigue loading remain unchanged. Measurement of the crystallite size of the HPT processed samples in dependency with loading cycles to failure as performed by using Convolutional Multiple Whole Profile (CMWP) [51,52] indicated a sub-grain size of about 20 nm for all specimens. These data also confirm absence of grain coarsening as a result of dynamic recrystallization of the UFG Ti-45Nb during the high cycle fatigue.

The influence of cyclic loading on the evolution of nanohardness and dislocation density ( $\rho$ ) of the UFG samples is displayed in Fig. 17 in which a gradual decrease of the both values with increasing the loading cycles is observed. The relatively high dislocation density of the Ti-45Nb sample after HPT processing ( $\rho = 2.1 \times 10^{15} \text{ m}^{-2}$ ) decreases about 10% after  $3.45e7$  loading cycles at 203 MPa and falls to about 60% of the original value ( $1.9 \times 10^{15} \text{ m}^{-2}$ ) after loading at 200 MPa and  $1e9$  loading cycles. The nanohardness values obtained for the same samples showed a slight reduction of about 4% in the intermediate regime and 12% at very high loading cycles.

Previous studies have shown that the decrease in hardness of UFG Cu after fatigue does not necessarily scale with the cell size according to a well-known relationship between the saturation stress and cell size [53]. It has been suggested that cyclic softening in UFG metals is not directly related to the grain coarsening and the mechanism of softening is related to the decrease of defect density and changes of boundary misorientation rather than to the grain size [54]. This might also be considered as a possible explanation of the moderate fatigue response of the UFG Ti-45Nb material of this study requiring future investigations.

## 5. Conclusion

The mechanical properties and high cycle fatigue performance of  $\beta$ -type Ti-45Nb alloy with conventional (CG) and ultrafine grained (UFG) microstructure were investigated by using small scaled samples with different geometries. The Ti-45Nb samples processed by HPT showed a considerable increase of hardness and strength due to the significant grain refinement while maintaining a low Young's modulus of about 65 GPa. Ultrasonic fatigue tests were conducted to obtain lifetime curves for the CG and UFG miniaturized samples which were plotted by using the calculated volume averaged stress against loading cycles to

failure. Based on the fatigue experiments on smooth and notched CG samples, Ti-45Nb alloy was found to be a notch sensitive material. Furthermore, only a slight improvement of the fatigue resistance of the UFG material with superior tensile properties was achieved. In order to explain this unexpected behavior, careful microstructural and texture analysis were performed which confirmed the microstructural stability of the UFG Ti-45Nb alloy and absence of grain coarsening up to the very high cycle regime. Cyclic softening effects were found in terms of a gradual reduction of hardness and dislocation density with increasing the loading cycles from  $1e6$  to  $1e9$ . According to our findings, the moderate fatigue performance of the UFG Ti-45Nb is more likely related to the early crack initiation due to the geometrical effects in the notch sensitive alloy and the rapid crack growth which is known as a common feature in nano- and ultrafine grained materials.

## Acknowledgments

The authors gratefully acknowledge E. Schafner from Faculty of Physics, University of Vienna for CMWP-Analysis and A. Steiger-Thirsfeld and S. Schwarz from USTEM at TU-Vienna for TEM images.

## References

- [1] M. Niinomi, *Metall. Mater. Trans. A* 33A (2002) 477–486.
- [2] Y. Okazaki, K. Kyo, Y. Ito, E. Nishimura, T. Tateishi, *Mater. Jpn.* 36 (1997) 1092–1099.
- [3] H. Hamanaka, T. Tsuchiya, *Feramu Jpn.* 2 (1997) 30–35.
- [4] T. Akahori, M. Niinomi, H. Fukui, M. Ogawa, H. Toda, *Mater. Sci. Eng.: C* 25 (3) (2005) 248–254.
- [5] N. Sumitomo, K. Noritake, T. Hattori, K. Morikawa, S. Niwa, K. Sato, M. Niinomi, *J. Mater. Sci.: Mater. Med.* 19 (4) (2008) 1581–1586.
- [6] M. Niinomi, INTECH Open Access Publisher, 2011.
- [7] Y. Song, D.S. Xu, R. Yang, D. Li, W.T. Wu, Z.X. Guo, *Mater. Sci. Eng. R.* 36 (2002) 143.
- [8] R. Godley, D. Starosvetsky, I. Gotman, 7, 2006, pp. 63–67.
- [9] M. Niinomi, T. Hattori, K. Morikawa, T. Kasuga, A. Suzuki, H. Fukui, S. Niwa, *Mater. Trans.* 43 (2002) 2970–2977.
- [10] M. Niinomi, *JOM* 51 (1999) 32–34.
- [11] M. Niinomi, T. Hattori, K. Morikawa, T. Kasuga, A. Suzuki, H. Fukui, S. Niwa, *Mater. Trans.* 43 (2002) 2970–2977.
- [12] T. Ozaki, H. Matsumoto, S. Hanada Watanabe, *Mater. Trans.* 45 (2004) 2776–2779.
- [13] J. Sun, Q. Yao, H. Xing, W.Y. Guo, *J. Phys.: Condens. Matter* 19 (2007) 486215.
- [14] H. Ikehata, N. Nagasako, T. Furuta, A. Fukumoto, K. Miwa, T. Saito, *Phys. Rev. B* 70 (2004) 174113.
- [15] B.A. Hatt, V.G. Rivlin, *Br. J. Appl. Phys.* 1 (1968) 1145–1149.
- [16] J. Jiang, A.Ma.F. Czerwinski, *InTech* (2011).
- [17] T.G. Langdon, *Acta Mater.* 61 (2013) 7035–7059.
- [18] G. Khatibi, J. Horky, B. Weiss, M.J. Zehetbauer, *Int. J. Fatigue* 32 (2) (2010) 269–278.
- [19] A. Vinogradov, S. Hashimoto, 5(5), 2003, pp. 351–358.
- [20] H.W. Höppel, M. Prell, L. May, M. Göken, *Procedia Eng.* 2 (1) (2010) 1025–1034.
- [21] H. Mughrabi, H.W. Höppel, 32(9), 2010, pp. 1413–1427.
- [22] R. Valiev, Yu.V. Zivanisenko, E.F. Rauch, B. Baudelet, *Acta Mater.* 44 (1996) 4705–4712.
- [23] G. Ribárik, Eotvos Lorand University, Budapest, 2008, pp. 42–72.
- [24] G. Ribárik, J. Gubicza, T. Ungár, *Mater. Sci. Eng. A* (2004) 343–387.
- [25] T. Ungár, G. Tichy, J. Gubicza, R. Hellmig, *J. Powder Diffr.* 20 (2005) 366.
- [26] T. Ungár, L. Balogh, G. Ribárik, *Mater. Sci. Forum* 584 (2008) 571–578.
- [27] W.C. Oliver, G.M. Pharr, *Mater. J. Res.* 7 (1992) 1564–1583.
- [28] M. Anwender, B. Zagar, B. Weiss, H. Weiss, *Exp. Mech.* 40 (2000) 1–8.
- [29] M. Papakyriacou, H. Mayer, C. Pypen, H. Plenk, S. Stanzl-Tschegg, *Mater. Sci. Eng.: A* 308 (1–2) (2001) 143–152.
- [30] W.D. Pilkey, *Peterson's Stress Concentration Factors*, 2nd ed., Wiley, New York, 1997.
- [31] P. Lukáš, L. Kunz, M. Svoboda, *Mater. Sci. Eng.: A* 391 (1) (2005) 337–341.
- [32] Y. Weixing, X. Kaiquan, G. Yi, On the fatigue notch factor, *Kf, Int. J. Fatigue* 17 (4) (1995) 245–251.
- [33] P. Lukáš, L. Kunz, M. Svoboda, *Mater. Sci. Eng.: A* 391 (1–2) (2005) 337–341.
- [34] M. Delshadmanesh, G. Khatibi, M. Lederer, M. Zehetbauer, H. Danninger, *Solid State Phenom.* 258 (2017) 337.
- [35] P. Grad, B. Reuscher, A. Brodyanski, M. Kopnarski, E. Kerscher, *Scr. Mater.* 67 (10) (2012) 838–841.
- [36] K. Dai, L. Shaw, *Int. J. Fatigue* 30 (8) (2008) 1398–1408.
- [37] I.P. Semenova, S.A. Gatina, V.S. Zhermakov, M. Janecek, in: *Proceedings of the 13th World Conference on Titanium*, John Wiley & Sons, Inc., pp. 1777–1781.
- [38] R.B. Figueiredo, E.R.D.C. Barbosa, X. Zhao, X. Yang, X. Liu, P.R. Cetlin, T.G. Langdon, *Mater. Sci. Eng.: A* 619 (2014) 312–318.

- [39] M. Launey, S.W. Robertson, L. Vien, K. Senthilnathan, P. Chintapalli, A.R. Pelton, J. Mech. Behav. Biomed. Mater. 34 (2014) 181–186.
- [40] S.J. Li, M. Niinomi, T. Akahori, T. Kasuga, R. Yang, Y.L. Hao, Biomaterials 25 (17) (2004) 3369–3378.
- [41] K. Hockauf, T. Niendorf, S. Wagner, T. Halle, L.W. Meyer, Procedia Eng. 2 (1) (2010) 2199–2208.
- [42] A. Vinogradov, J. Mater. Sci. 42 (2007) 1797–1808.
- [43] C.Z. Xu, Q.J. Wang, M.S. Zheng, J.W. Zhu, J.D. Li, M.Q. Huang, et al., Mater. Sci. Eng. A 459 (2007) 303–308.
- [44] H.W. Höppel, Mater. Sci. Forum 503–504 (2006) 259–266.
- [45] R.H. Li, Z.J. Zhang, P. Zhang, Z.F. Zhang, Acta Mater. 61 (15) (2013) 5857–5868.
- [46] M. Niinomi, Low Modulus Titanium Alloys for Inhibiting Bone Atrophy, Biomaterials Science and Engineering, in: Rosario Pignatello (Ed.), InTech, 2011, <http://dx.doi.org/10.5772/24549>.
- [47] S. Suresh, Fatigue of Materials, 2nd ed., Cambridge University Press, Cambridge, 1998.
- [48] I.C. Choi, B.G. Yoo, O. Kraft, R. Schwaiger, M.Y. Seok, M. Kawasaki, J.I. Jang, Mater. Sci. Eng.: A 618 (2014) 37–40.
- [49] Warren Young, Richard Budynas, Roark's Formulas for Stress and Strain, 8th ed., McGraw-Hill, 2011.
- [50] K. Yang, Yu Ivanisenko, A. Caron, A. Chuvilin, L. Kurmanaeva, T. Scherer, R.Z. Valiev, H.-J. Fecht, Acta Mater. 58 (3) (2010) 967–978.
- [51] G. Ribárik, T. Ungár, J. Gubicza, J. Appl. Cryst. 34 (2001) 669–676.
- [52] T. Ungár, J. Gubicza, G. Ribárik, A. Borbély, J. Appl. Cryst. 34 (2001) 298–310.
- [53] L.F. Kunz, Mechanical Properties of Copper Processed by Severe Plastic Deformation, Copper Alloy-Early Applications and Current Performance-Enhancing Processes, in: Luca Collini (Ed.), InTech, 2012, <http://dx.doi.org/10.5772/32634>.
- [54] I. Sabirov, Y. Estrin, M.R. Barnett, I. Timokhina, P.D. Hodgson, Acta Mater. 56 (10) (2008) 2223–2230.